

Structural phase diagram for Sm-substituted BiFeO₃ multiferroicsV. Petkov ^{1,*}, A. Zafar ¹, L. Gallington ², S. Shastri ² and B. Aoun ³¹Department of Physics, Central Michigan University, Mount Pleasant, Michigan 48858, USA²X-Ray Science Division, Advanced Photon Source, Argonne National Laboratory, Argonne, Illinois 60439, USA³fullrnc LLC, Dallas, Texas 75002, USA

(Received 19 July 2024; accepted 20 November 2024; published 13 December 2024)

The structural evolution of Sm substituted BiFeO₃ is studied by total x-ray scattering and structure modeling. It is shown that the crystal structure changes from polar to antipolar and then to nonpolar when the Sm to Bi ratio in the material approaches 20% and 40%, respectively, with no intermixing between the structure types. The evolution is driven by lattice strain induced by the difference in the size of Sm and Bi atoms, leading to changes in the pattern of octahedral tilts and Bi off-centering, which, in turn, induce changes in the multiferroic properties. The substitution ratio at which the different structure types emerge appears to be tied up with the average radius of the atomic species occupying the Bi sites in the perovskite lattice and volume occupied by a formula unit, rendering both quantities useful predictor variables for guiding computational searches for substituted BiFeO₃ multiferroics with improved functional properties.

DOI: [10.1103/PhysRevMaterials.8.124407](https://doi.org/10.1103/PhysRevMaterials.8.124407)

I. INTRODUCTION

Chemical substitution is a key tunable parameter for improving the properties of functional materials [1–9]. An archetypal example is the rare earth (RE) substituted BiFeO₃ (BFO) system. Pure BFO is unique among the multiferroic materials because it exhibits coexisting magnetic and ferroelectric (FE) orders at room temperature, providing an opportunity to control its properties using magnetic and/or electric field [10–13]. At room temperature, it adopts a rhombohedral space group (S.G.) *R3c* structure, featuring a perovskite network of corner-sharing Fe–O₆ octahedra with Bi atoms sitting in the cavities between the octahedra. Contrary to the aristotype cubic perovskite, the octahedra are rotated in an antiferrodistortive manner and both Bi and Fe atoms are displaced from their positions in the cubic perovskite, as shown in Fig. 1(a). Due to a strong interaction between the O *2p* orbitals and lone pair of Bi *6s*² electrons, the largely ionic bonding between Bi³⁺ and O^{2–} ions has a partial covalent character leading to a considerable Bi off-centering that is considered to be behind the ferroelectricity in BFO. On the other hand, the magnetic order arises from antiferromagnetic (AFM) superexchange interactions between the spins of nearby Fe atoms. Due to antisymmetric Dzyaloshinskii-Moria (DM) interactions, the spins are weakly canted away from the AFM axis, leading to the appearance of weak ferromagnetism. The net magnetization, however, is zero, due to the presence of a spiral spin modulation superimposed on the AFM structure, which negates the linear coupling between the polarization and magnetization in BFO, hampering practical applications [14–19].

It has been shown that the substitution of Bi for light RE species both disturbs the spin spiral and reduces the formation of oxygen vacancies in BFO leading to the emergence of nonzero net magnetization and stabilization of the electrical polarization, respectively, thus facilitating practical applications [4,20–25]. The structural mechanism behind the improved magnetic and ferroelectric properties of light RE substituted BFO, however, remains unclear. In general, it is associated with the emergence of new phases induced by changes in the average radius, $\langle r \rangle_A$, of the *A*-type atomic species in the *ABO*₃ perovskite lattice and related to it changes in the Goldschmidt tolerance factor, where the changes arise from the difference in the size of substituted Bi and substituent RE species [e.g., $r(\text{Bi}^{3+}) = 1.37 \text{ \AA}$ vs $r(\text{La}^{3+}) = 1.36 \text{ \AA}$, $r(\text{Pr}^{3+}) = 1.32 \text{ \AA}$, $r(\text{Nd}^{3+}) = 1.29 \text{ \AA}$, and $r(\text{Sm}^{3+}) = 1.28 \text{ \AA}$ for 12-fold coordination] [26,27]. The reported sequence of phase transitions and emerging new phases with increasing RE content are, however, not well established even in the case of La substituted BFO, where the changes in $\langle r \rangle_A$ appear small [Fig. 1(b)]. In particular, several studies have suggested that La substituted BFO undergoes a sequence of phase transitions with La content from a polar S.G. *R3c* structure to a polar S.G. *C222* structure, followed by a transition to a polar S.G. *Pna2*₁ structure, nonpolar S.G. *Imma*, or nonpolar S.G. *Pbnm* structure, where the latter two cannot harbor ferroelectric order. The presence of intermixing of these phases over broad composition ranges has also been suggested [28–33]. However, our recent total x-ray scattering studies showed that the substitution of Bi for La up to a level of 40% does not induce distinct phase transitions and segregation. Rather, it leads to an overall distortion of the crystal lattice such that its average symmetry is reduced to triclinic, but, locally, the rhombohedral symmetry relationship between the positions of the constituent atoms remains [34]. The situation with the smaller in size RE species such as, for example, Sm, is more

*Contact author: petko1vg@cmich.edu

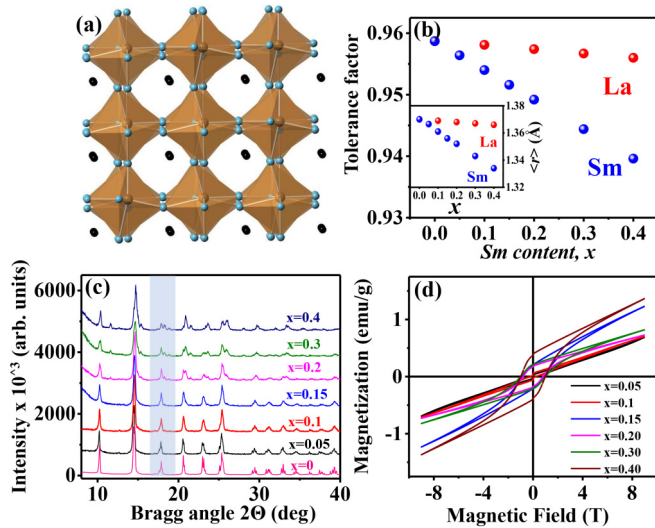


FIG. 1. (a) Fragment from the rhombohedral structure of BiFeO₃, featuring corner-sharing Fe (brown circles)–oxygen (blue circles) octahedra with Bi (dark red circles) atoms positioned in the cavities between them. The octahedra are rotated with respect to each other and Bi atoms are displaced from the geometrical center of the cavities, rendering the material ferroelectric. (b) Goldschmidt tolerance factor and average A-type cation size $\langle r \rangle_A$ for Sm_xBi_{1-x}FeO₃. For comparison, data for La_xBi_{1-x}FeO₃ are also shown. (c) XRD patterns for Sm_xBi_{1-x}FeO₃, where $x = 0.0, 0.05, 0.1, 0.15, 0.2, 0.3,$ and 0.4 . Blue rectangle highlights the evolution of Bragg peaks with Sm content. The evolution is shown on an expanded scale in Fig. S1. (d) Room temperature magnetic hysteresis curves for Sm_xBi_{1-x}FeO₃.

complicated because $\langle r \rangle_A$ diminishes much faster with their content [Fig. 1(b)]. The situation is further exacerbated by the fact that the transition between the polar S.G. *R3c* and nonpolar S.G. *Pbnm* structure adopted by the end members BFO and SmFeO₃, respectively, is symmetry forbidden, suggesting a possible coexistence of bridging phases. Then, it is not a surprise that several authors have reported that the S.G. *R3c* to S.G. *Pbnm* phase transformation in Sm_xBi_{1-x}FeO₃ occurs over a broad composition range extending from $x \sim 0.1$ to $x \sim 0.25$ [35–37], with variable levels of phase coexistence between the two symmetries observed in the intermediary composition range. Other studies have reported the emergence of an intermediate antipolar PbZrO₃ type (S.G. *Pbam*) phase in a narrow composition window between the S.G. *R3c* and S.G. *Pbnm* phases that is centered at about $x = 0.15$, including a coexistence of S.G. *R3c*, S.G. *Pbam*, and S.G. *Pbnm* phases [20,38,39]. The emergence of a nonpolar S.G. *Imma* bridging phase has also been suggested [40,41].

Here we address the ambiguity by employing total and resonant synchrotron x-ray scattering coupled to computer modeling to reveal the evolution of the crystal structure in Sm_xBi_{1-x}FeO₃ when x varies from 0.0 to 0.4. Similar to the case of La substituted BFO, we find that, locally, Sm substituted BFO preserves its polar S.G. *R3c* structure for $x \leq 0.15$. Contrary to the case of La substituted BFO, Sm_xBi_{1-x}FeO₃ is found to undergo a phase transition to a locally antipolar, S.G. *Pnam*-type structure when x approaches 0.2. When x approaches 0.4, a locally nonpolar, S.G. *Pbnm*-type structure

emerges [42]. Notably, due to the large difference between the size of Bi and Sm species, Sm_xBi_{1-x}FeO₃ perovskites appear to exhibit an overall triclinic lattice distortion which seamlessly bridges the polar, antipolar and nonpolar phases emerging with increasing x . The results explain the evolution of ferroelectric and magnetic properties of Sm substituted BFO without evoking a phase segregation scenario and may serve as a structural basis for exploring RE substituted BFO for piezoelectric and supercapacitor applications. They also highlight the correspondence between chemical substitution induced and temperature induced lattice distortions in RE substituted BFO, including the phase transitions caused by them.

II. EXPERIMENT

A. Sample preparation

Polycrystalline Sm_xBi_{1-x}FeO₃ samples, where $x = 0, 0.05, 0.1, 0.15, 0.2, 0.3,$ and 0.4 , were prepared by a traditional solid-state synthesis using stoichiometric amounts of Bi₂O₃ (99.999%), Fe₂O₃ (99.999%), and Sm₂O₃ (99.9%). The starting materials were intermixed, thoroughly ground, calcined at 980 K for 8 h, and then annealed at 1170 K for two days. High-resolution powder diffraction patterns obtained on in-house equipment are shown in Fig. 1(c). As shown below, the pattern for pure BFO was successfully fit with a model based on a rhombohedral S.G. *R3c* structure, attesting to its phase purity. The XRD patterns for Sm substituted BFO samples are seen to show increasingly distinct features with Sm content [see the light blue shaded area in Fig. 1(c) and Fig. S1 in the Supplemental Material [43]], indicating the presence of significant changes in the atomic arrangement. The changes are discussed below.

B. Magnetic properties characterization

Magnetic properties of the samples were studied on a physical property measuring system (PPMS) at room temperature. Experimental data are shown in Fig. 1(d). As expected, pure BFO does not show any magnetic hysteresis, which is typical for AFM materials. The samples containing Sm show increasingly broad magnetic hysteresis with Sm content that exhibits a significant remanent and saturation magnetization. The result confirms that the spin cycloid in Sm substituted BFO is increasingly suppressed with Sm content, allowing the weak ferromagnetism in BFO to emerge.

C. Synchrotron total x-ray scattering experiments

Total x-ray scattering experiments were conducted at the beamline 1-ID-E, Argonne National Laboratory, using x rays with energy of 90.024 keV ($\lambda = 0.1376$ Å), which is 500 eV below the *K* edge of Bi (90.524 keV). The use of higher-energy x rays is essential for collecting data to high wave vectors, q (in our case $q_{\max} = 25$ Å⁻¹), which is necessary for obtaining high-resolution atomic pair distribution functions (PDFs). Samples were packed in thin Kapton tubes and scattered intensities were recorded with a single-photon-counting PilatusX CdTe 2M detector. A representative two-dimensional (2D) diffraction image for Si standard used to calibrate the

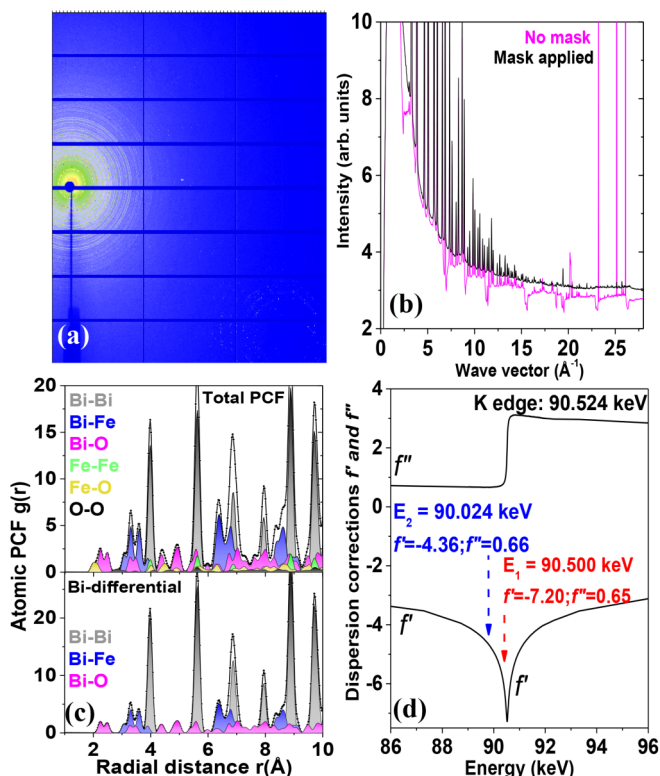


FIG. 2. (a) 2D diffraction image for Si standard obtained with a PilatusX CdTe 2M detector made of 24 CdTe sensor tiles. The tiles are separated by one-pixel wide gaps appearing as horizontal and vertical lines in the image. (b) XRD patterns for Si standard obtained from the 2D image in (a) with (black) and without (magenta) masking the gaps and overexposed pixels. Unphysical sharp dips and spikes are present in the “unmasked” XRD data. (c) Computed total and Bi-differential atomic pair correlation functions (PCFs) $g(r) = \rho(r)/\rho_o$ (black) for pure BiFeO_3 . The individual partial PCFs are also shown, each in a different color. Note that, as defined, the PCF $g(r) = \rho(r)/\rho_o$ oscillates about 1 while the PDF $G(r) = 4\pi r \rho_o [\rho(r) - 1]$ oscillates about zero. (d) Energy dependence of the real f' and imaginary f'' dispersion corrections to the x-ray scattering factor for Bi. The energies below the K edge of Bi used in the present experiments are marked with arrows. Values for f' and f'' at these energies are also given.

detector is shown in Fig. 2(a). One dimensional (1D) x-ray diffraction (XRD) patterns derived from the image are shown in Fig. 2(b). As can be seen in Fig. 2(a), one-pixel-wide gaps exist between the detector tiles which, if not accounted for, would corrupt the 1D XRD patterns [red curve in Fig. 2(b)], rendering them unsuitable for crystal structure studies. When the gaps are properly masked, as done here, high quality 1D XRD patterns are obtained [black curve in Fig. 2(b)]. A representative high-quality XRD pattern for $\text{Sm}_{0.1}\text{Bi}_{0.9}\text{FeO}_3$ is shown in Fig. 3(a). After due corrections for background scattering and sample absorption, the corrected XRD intensities $I(q)$ were converted to a so-called structure function, $S(q)$, defined as

$$S(q) = \frac{I(q) - [\langle f^2(q) \rangle - \langle f(q) \rangle^2]}{\langle f(q) \rangle^2} = \frac{I(q) - \langle f^2(q) \rangle}{\langle f(q) \rangle^2} + 1, \quad (1)$$

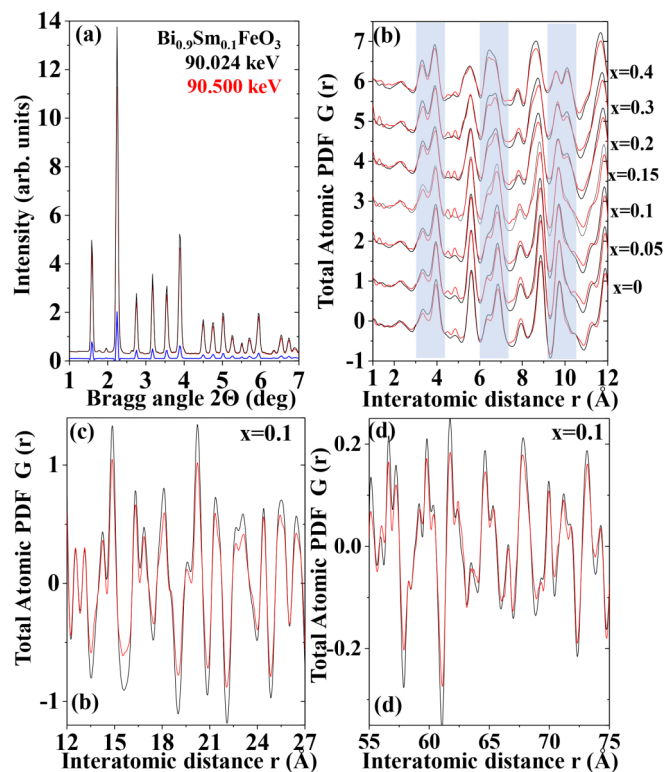


FIG. 3. (a) XRD patterns for $\text{Sm}_{0.1}\text{Bi}_{0.9}\text{FeO}_3$ taken at 25 eV (red) and 500 eV (black) below the K edge of Bi (90.524 keV). Their difference (blue) multiplied by a factor of 3 is also shown. (b) Total (black) and Bi-differential (black) PDFs for $\text{Sm}_x\text{Bi}_{1-x}\text{FeO}_3$, $x = 0, 0.05, 0.1, 0.15, 0.2, 0.3$, and 0.4 . Blue rectangles highlight the marked evolution of selected PDF peaks with Sm content. (c), (d) Comparison between the total and Bi-differential PDF for $\text{Sm}_{0.1}\text{Bi}_{0.9}\text{FeO}_3$ over an extended range of interatomic distances.

where $\langle f(q) \rangle^2 = [\sum c_i f_i(q, E)]^2$ and $\langle f(q)^2 \rangle = \sum c_i f_i^2(q, E)$. Here c_i is the concentration of i -type atomic species, $f(q) = f_o(q) + f'(q, E) + i f''(q, E)$ is the x-ray atomic scattering factor, q is the magnitude of the wave vector ($q = 4\pi \sin\theta/\lambda$), 2θ is the angle between the incoming and outgoing x rays, λ is the wavelength of the x rays used, and $f'(q, E)$ and $f''(q, E)$ are the so-called dispersion corrections to $f(q)$. A total atomic PDF $G(r)$ for $\text{Sm}_{0.1}\text{Bi}_{0.9}\text{FeO}_3$ derived from the $S(q)$ via a Fourier transformation is shown in Fig. 3(b). Total $G(r)$'s for all other samples, derived as described above, are also shown in Fig. 3(b). The derivation of $S(q)$'s and $G(r)$'s was done with the help of an improved version of the software RAD [44].

By definition, $G(r) = 4\pi r [\rho(r) - \rho_o]$, where $\rho(r)$ and ρ_o are the local and average atomic number density, respectively, and r is the radial distance. The PDFs in Fig. 3(b) exhibit a series of well-defined peaks at interatomic distances where the local atomic density exceeds the average one, i.e., where well-defined interatomic distances in the studied material appear. Several of the peaks are seen to change systematically with Sm content (light blue shaded areas), directly reflecting the rearrangement of constituent atoms in $\text{Sm}_x\text{Bi}_{1-x}\text{FeO}_3$ taking place when Bi is substituted for Sm species. Here it is to be noted that atomic PDFs take into account both Bragg peaks

and the diffuse component of the diffraction data and, hence, are sensitive to both the average crystal structure and local deviations from it, including lattice distortions in perovskites arising from chemical substitution [45–52].

D. Resonant x-ray scattering experiments at the K edge of Bi

As obtained from a single diffraction experiment, e.g., by using x rays with energy of 90.024 keV in our case, total PDFs reflect all chemically distinct correlations between the constituent atoms in the studied material, as follows:

$$G(r) = \sum_{i,j} w_{ij}(q)G_{ij}(r), \quad (2)$$

where $G_{ij}(r)$ are known as partial PDFs and the so-called weighting factors $w_{ij}(q)$ are defined as

$$w(q)_{ij} = \frac{c_i f_i(q, E) c_j f_j(q, E)}{\langle f(q) \rangle^2}. \quad (3)$$

In the case of pure BFO, there are six partial $G_{ij}(r)$ reflecting Bi-Bi, Bi-Fe, Bi-O, Fe-Fe, Fe-O, and O-O pair correlations. Typically, the correlations overlap heavily, as shown in Fig. 2(c), making it difficult to interpret total PDF data unambiguously. To obtain structure data with an increased sensitivity to atomic correlations involving the ferroactive Bi atoms, for all samples, we collected a second XRD pattern using x rays with energy of 90.500 keV ($\lambda = 0.1368 \text{ \AA}$) that is 24 eV below the K edge of Bi. The significant intensity difference between the patterns obtained using x rays with energy $E_1 = 90.024 \text{ keV}$ and $E_2 = 90.500 \text{ keV}$ [Fig. 3(a)] comes from the difference in the atomic scattering factors of Bi atoms for the two energies, which largely arise from differences in the dispersion corrections $f'(q, E)$ and $f''(q, E)$ [see Fig. 2(d)]. From the two data sets, so-called differential structure functions, $DS(q)_A$, defined as

$$DS(q)_A = \frac{I(q, E_1) - I(q, E_2) - [\langle f^2(E_1) \rangle - \langle f^2(E_2) \rangle]}{\langle f(E_1) \rangle^2 - \langle f(E_2) \rangle^2} + 1, \quad (4)$$

were computed and Fourier transformed into Bi-differential PDFs $DG(r)_{Bi}$. As obtained, the latter appear as a weighted average only of correlations involving Bi atoms, that is, only Bi-Bi, Bi-Fe, and Bi-O correlations in the case of pure BFO, as follows:

$$DG(r)_{Bi} = \sum_i \Delta w_{Bi,j} G_{Bi,j}(r), \quad (5)$$

where the weighting factors are defined as

$$\Delta w_{Bi,j} = \frac{c_j f_j(q, E)}{\langle f(q, E) \rangle} \quad (6)$$

and $j = \text{Bi, Fe, and O}$. As such, Bi-differential PDFs provide an extra, Bi environment-specific data set for the structure modeling described below. The Bi-differential PDFs for studied $\text{Sm}_x\text{Bi}_{1-x}\text{FeO}_3$ perovskites are shown in Fig. 3(b). Differences between total and Bi-differential PDFs are highlighted in Figs. 3(c) and 3(d) over an extended range of interatomic distances. More details about resonant x-ray scattering experiments can be found in Refs. [34,53–56].

III. STRUCTURE MODELING

A. Crystal structure assessed by Rietveld analysis

The major difference between the suggested structure types for pure and RE substituted BFO is the pattern of octahedral tilts and coupled to them Bi atom off-centering, including changes in the crystal structure polarity and unit cell parameters. In the polar S.G. $R3c$ -type structure of pure BiFeO_3 , Fe-O_6 octahedra exhibit antiferrodistortive (Glaser notation $a^-a^-a^-$) tilts and the rhombohedral lattice parameter is essentially the a_c parameter of the aristotype cubic perovskite. In the nonpolar S.G. $Pbnm$ structure of SmFeO_3 orthoferrite, Fe-O_6 octahedra exhibit out-of-phase tilts in the a and b planes of the orthorhombic lattice and in-phase tilts along the c axis, corresponding to the $(a^-a^-c^+)$ Glaser notation [57], while the orthorhombic lattice parameters (a, b, c) appear as $a = \sqrt{2}a_c$, $b = \sqrt{2}a_c$, and $c = 2a_c$. It is recognized that the introduction of Sm in BFO induces lattice distortions, which, according to some studies [58], reduce the average crystal symmetry to antipolar S.G. $Pbam$ (PbZrO_3)-type for $0.1 \leq x \leq 0.2$ [59], where the tilting of Fe-O_6 octahedra may be described in terms of the $(a^-a^-c^o)$ Glaser notation and the orthorhombic lattice parameters appear as $a = \sqrt{2}a_c$, $b = 2\sqrt{2}a_c$, and $c = 2a_c$. A number of studies suggest that the symmetry is indeed reduced to an antipolar S.G. $Pnam$ (NaNbO_3)-type, where the complex tilting pattern of Fe-O_6 octahedra is a combination of $(a^-a^-c^+)$ - and $(a^-a^-a^-)$ -type tilts, while the lattice parameters appear as $a = \sqrt{2}a_c$, $b = 2\sqrt{2}a_c$, and $c = 4a_c$ [59]. Other studies suggest that, together with a S.G. $Pbam$ type phase, a $\text{Sm}_x\text{Bi}_{1-x}\text{O}_3$ phase with a nonpolar S.G. $Imma$ -type structure ($a^o b^- b^-$ octahedral tilts) appears for $0.1 \leq x \leq 0.25$ [40,41].

To assess the tilt pattern and related polarity of the crystal structure for $\text{Sm}_x\text{Bi}_{1-x}\text{O}_3$, both of which are important for the ferroelectric properties, we carried out Rietveld analysis of the XRD patterns. The analysis was performed using software FULLPROF [60]. At first, the XRD patterns for the samples with $x \leq 0.15$ were fit with a model based on the rhombohedral S.G. $R3c$ type structure of pure BFO. As expected, the model (10 refinable parameters; see Table S1 in [43]) reproduced very well the XRD pattern for pure BFO [Fig. 4(a)], which was not the case with the $\text{Sm}_x\text{Bi}_{1-x}\text{O}_3$ samples where $x = 0.05, 0.1, \text{ and } 0.15$ [Figs. 4(b), 4(c), and 4(d)]. Moreover, the rhombohedral S.G. $R3c$ model completely failed to reproduce the XRD data for $\text{Sm}_x\text{Bi}_{1-x}\text{O}_3$ samples with $x = 0.2, 0.3, \text{ and } 0.4$ [Figs. 5(a), 5(b), and 5(c)]. The XRD data for the samples with $x = 0.2$ and 0.3 could not be fitted with the nonpolar S.G. $Pbnm$ model (14 refinable parameters; see Table S1) either [Figs. 5(d) and 5(e)]. By contrast, a fit based on the antipolar S.G. $Pbam$ model (22 refinable parameters; see Table S1) performed considerably better [Figs. 5(g) and 5(h)]. On the other hand, the nonpolar S.G. $Pbnm$ model performed better [Fig. 5(i)] in the case of $\text{Sm}_{0.4}\text{Bi}_{0.6}\text{O}_3$ as compared to the antipolar S.G. $Pbam$ model [Fig. 5(f)]. Altogether, the results of Rietveld refinements showed that $\text{Sm}_x\text{Bi}_{1-x}\text{O}_3$ is likely to be rhombohedral for $x \leq 0.15$ and orthorhombic for $x > 0.15$, where the atomic arrangement changes to nonpolar as x approaches 0.4. Because of the poor overall quality of single-phase Rietveld fits (goodness-of-fit factors considerably larger than 10%; see Fig. 5), prior studies have

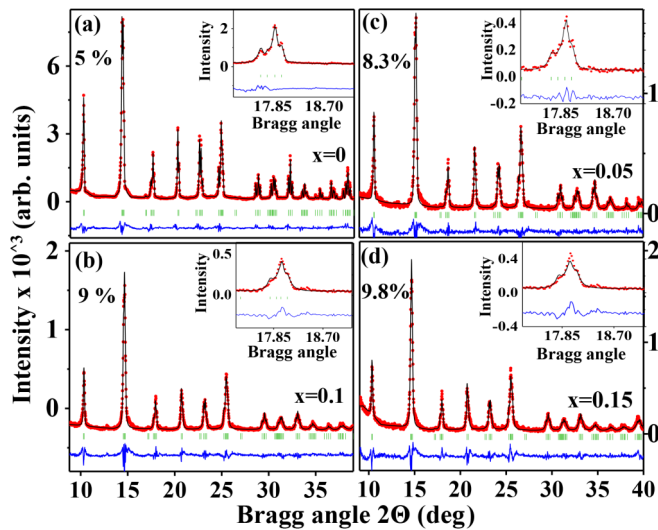


FIG. 4. Rietveld fits (black) to XRD patterns (red) for $\text{Sm}_x\text{Bi}_{1-x}\text{FeO}_3$ ($x = 0.0, 0.05, 0.1, \text{ and } 0.15$) based on a S.G. $R3c$ model. Vertical green bars show the position of Bragg peaks. The residual difference (blue) is shifted downward for clarity. The goodness-of-fit indicator R_{wp} varies from 5% ($x = 0$) to 9.8% ($x = 0.15$), i.e., it deteriorates with Sm content. The insets show the model ability to reproduce the Bragg diffraction feature at 17.85° highlighted in Figs. 1(c) and S1.

successfully attempted two-phase fits [35–41] and suggested a phase segregation scenario for $\text{Sm}_x\text{Bi}_{1-x}\text{O}_3$ with $0.1 < x \leq 0.4$. This is not necessarily the case as our PDF modeling results show.

B. Crystal structure assessed by small-scale PDF modeling

To assess the crystal structure of Sm substituted BFO in a more precise manner, we analyzed the experimental total PDFs which are more sensitive to lattice distortions in comparison to the respective XRD patterns. Initially, we fit the PDFs with the structure models explored by Rietveld analysis, which feature a single crystallographic unit cell. The fits were done with the help of the software PDFGUI [61], where the so-called instrumental resolution parameters q_{damp} and q_{broad} were given values of 0.013 and 0.023, as determined by measuring and analyzing a Si powder standard. As shown in previous studies [34,62] and confirmed here [Fig. S2(a)], the total PDF for pure BFO can be well fit with a rhombohedral S.G. $R3c$ type model. The model fits well the PDF data for BFO [see Fig. S2(a)], but did not perform well in the case of $x = 0.05, 0.1, \text{ and } 0.15$ samples [see Figs. S2(b), S2(c), and S2(d)]. Furthermore, the rhombohedral model completely failed to reproduce the PDFs for $\text{Sm}_x\text{Bi}_{1-x}\text{O}_3$ samples with $x > 0.2$ [e.g., see Figs. S3(a) and S4(a)]. The PDF for $\text{Sm}_{0.2}\text{Bi}_{0.8}\text{O}_3$ was attempted to be fit by models based on the nonpolar S.G. $Imma$ and S.G. $Pbnm$ structures, which failed as data in Figs. S3(b) and S3(d) show. The antipolar S.G. $Pnam$ model performed somewhat better [Fig. S3(c)]. The model fits to the PDF for $\text{Sm}_{0.3}\text{Bi}_{0.7}\text{O}_3$ produced similar results. In the case of $\text{Sm}_{0.4}\text{Bi}_{0.6}\text{O}_3$, however, the nonpolar S.G. $Pbnm$ model performed better in comparison to the S.G. $Imma$ and S.G. $Pnam$ models (see Fig. S4). Overall, single unit cell-based

Rietveld and PDF analysis produced inconclusive results for the structure of $\text{Sm}_x\text{Bi}_{1-x}\text{O}_3$ samples with $x > 0.15$ largely because they did not take into account the likely presence of lattice distortions arising from the different size of Sm and Bi species. We accounted for the distortions as shown below.

In particular, prompted by the results of our study on La substituted BFO, we approached the PDFs for $\text{Sm}_x\text{Bi}_{1-x}\text{O}_3$ samples with $x \leq 0.15$ [Fig. 5(i)] with a model featuring a triclinically distorted rhombohedral lattice, hereafter referred to as a S.G. $R3c/P1$ -type model (14 refinable parameters; see Table S1), where the average rhombohedral symmetry of the crystal lattice is broken but the rhombohedral symmetry relationships between the atomic positions are preserved. Note that such a type of symmetry reduction is difficult to explore by Rietveld analysis. As can be seen in Figs. 6(a), 6(b), and 6(c), the model reproduced the experimental PDF data much better in comparison to the undistorted S.G. $R3c$ model [Figs. S2(b), S2(c), and S2(d)]. From all tested models, a triclinically distorted antipolar S.G. $Pnam/P1$ model refined best against the total PDFs for $x = 0.2$ and 0.3 samples [Figs. 6(d) and 6(e)], while the total PDF for the $x = 0.4$ sample was relatively well approximated by a model based on a triclinically distorted nonpolar S.G. $Pbnm/P1$ structure [Fig. 6(f)]. Notably, similar to the case of the S.G. $R3c/P1$ model, the lattice parameters and angles for the S.G. $Pnam/P1$ and S.G. $Pbnm/P1$ models are allowed to be refined independently while the respective symmetry relationship between the atomic sites in the unit cells are left intact. The results of small-scale PDF modeling where the average crystallographic symmetry is broken indicated that the atomic arrangement in Sm substituted BFO samples is BFO-like polar for $x \leq 0.15$, changes to an antipolar for $0.15 < x \leq 0.3$, and becomes orthoferritelike nonpolar when x approaches 0.4. Because single-phase models reproduce the experimental PDFs well, no phase segregation appears to take place for any $0 \leq x \leq 0.4$. Rather, the crystal structure experiences an overall triclinic distortion which bridges the evolving polar to an antipolar and then to a nonpolar atomic arrangement in $\text{Sm}_x\text{Bi}_{1-x}\text{FeO}_3$ with increasing Sm content. This structure description, however, remains incomplete because models based on a single crystallographic unit cell, be it distorted or not, consider that the significantly different in size Bi and Sm atoms occupy the same Wyckoff positions in the cell, i.e., the same size cavities in the perovskite lattice, ignoring the fact that lattice cavities occupied by the larger in size Bi species experience “negative” pressure from the nearby cavities filled with the smaller in size Sm species, and vice versa, which would inevitably generate a variety of local octahedral tilts and Bi off-centering patterns. Typically, crystallographic unit-cell-based models would represent this variety as abnormally increased thermal atomic vibrations, which may hinder the precise determination of atomic positions and arrangement pattern necessary for properties calculation and interpretation.

C. Crystal structure assessed by large-scale PDF modeling

To reveal the atomic structure for Sm substituted BFO in full detail, we constructed structure models representing

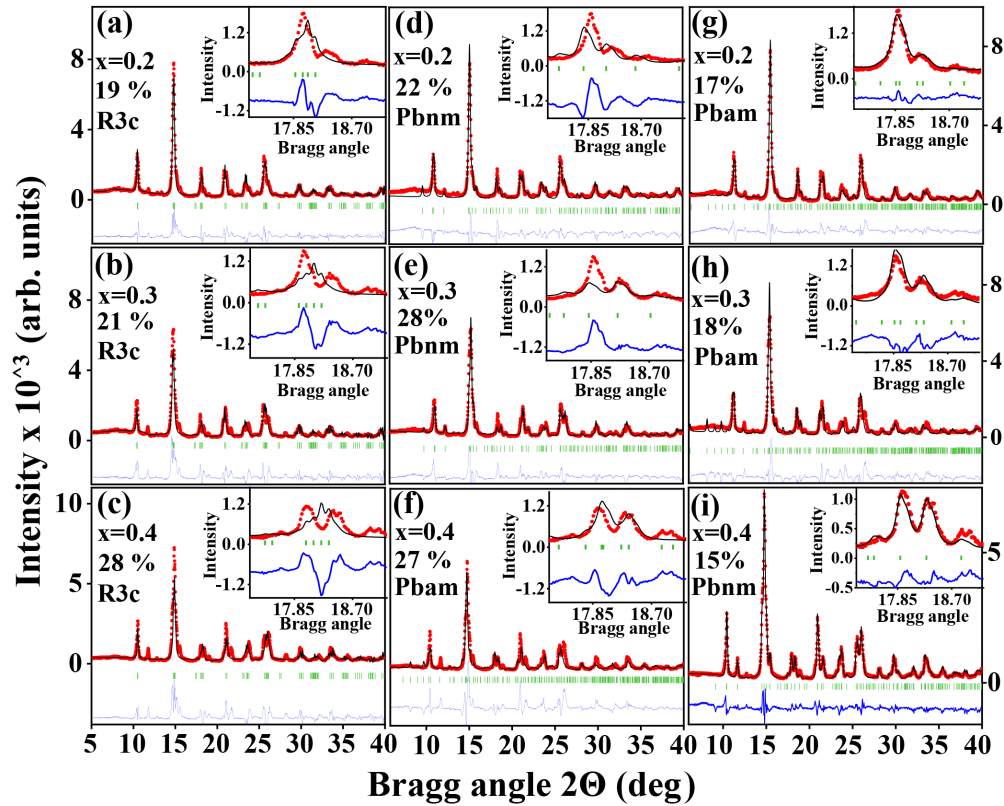


FIG. 5. Rietveld fits (black) to XRD patterns (red) for $\text{Sm}_x\text{Bi}_{1-x}\text{FeO}_3$ ($x = 0.2, 0.3,$ and 0.4) based on rhombohedral *S.G. R3c* and orthorhombic *S.G. Pbam* and *S.G. Pbnm* models. Vertical green bars show the position of Bragg peaks. The residual difference (blue) is shifted downward for clarity. The goodness-of-fit indicator R_{wp} is given for each data set in %. The insets show the ability of particular models to reproduce the Bragg diffraction feature at 17.85° highlighted in Figs. 1(c) and S1.

$150 \text{ \AA} \times 150 \text{ \AA} \times 150 \text{ \AA}$ configurations of about 330000 Bi, Sm, Fe, and oxygen atoms in due proportions, where each model appears as a perovskite lattice of the type shown in Fig. 1(a). The large size of the models allowed us to consider a statistically representative variety of distinct Sm and Bi atomic sites. The initial atomic configuration for pure BFO was generated using structure parameters resulting from the single unit-cell-based fit shown in Fig. S2(a). The initial atomic configurations for the samples with $x = 0.05, 0.1, 0.15, 0.2, 0.3,$ and 0.4 we generated using structure parameters resulted from the single unit-cell-based fits shown in Figs. 6(a)–6(f), respectively. The models were simultaneously refined against the respective total and Bi-differential PDFs by reverse Monte Carlo (RMC) simulations using software FULLRMC [63]. During the refinement, Bi, Sm, and oxygen atoms were constrained not to approach each other closer than the Bi-O and Sm-O distances in BiFeO_3 and SmFeO_3 perovskites, respectively, whereas Fe-O distances were allowed to range between 1.95 \AA and 2.15 \AA . In addition, Fe-oxygen and oxygen-Fe first coordination numbers were restrained to stay close to 6 and 2, respectively, thus preserving the connectivity of the modeled perovskite lattice. Initially, the atoms were moved with a step of 0.025 \AA , which was reduced to 0.01 \AA in the final stages of the modeling. For all compositions, it was terminated when no further improvement

in the quality of the model fits to the respective total and Bi-differential PDF was possible to be achieved, given the particular restraints and constraints applied. Notably, three model runs for each of the studied samples were conducted. Although the atomic configurations resulted from the runs did not differ greatly, the quantities extracted from them, including bond angles, atomic volume, and lattice polarization values reported below, were averaged out for the sake of improving the accuracy of the model results. The RMC refined models fit the experimental total and Bi-differential PDF for pure and Sm substituted BFO in fine detail over a range of interatomic distances including at least 10 crystallographic unit cells (see Figs. 7–10 and S5). Representative atomic configurations from the refined models are shown in Fig. 11. Here it is to be noted that initial RMC configurations based on crystallographic structure types that did not fit the experimental total PDFs well could not converge to large-scale models that reproduce the experimental total and Bi-differential PDFs well. The reason is that, currently, RMC algorithms may not change the lattice geometry of the initial atomic configuration, making it imperative to start the RMC modeling of crystal systems exhibiting lattice distortions from as realistic as possible initial configurations, such as, for example, configurations based on crystallographic unit-cell-based models tested and refined by preliminary Rietveld and/or PDF analysis, as done here.

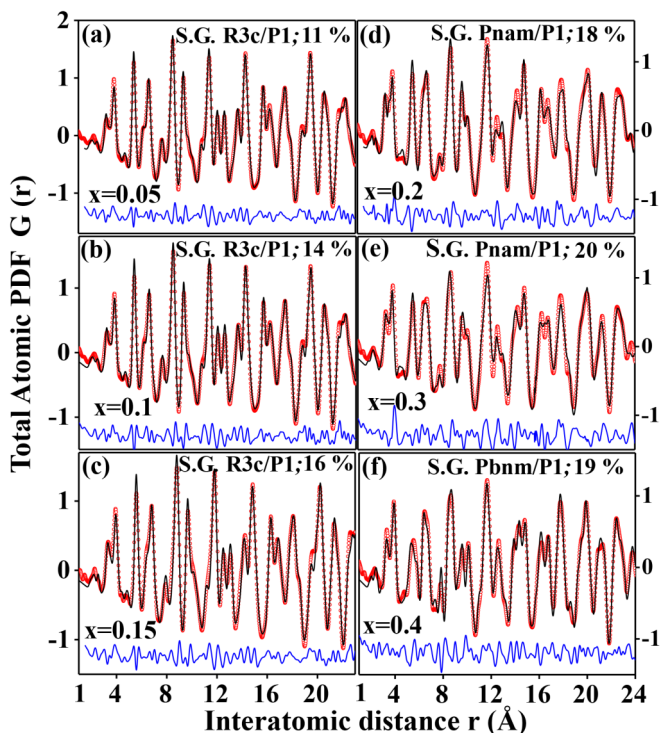


FIG. 6. Successful small-box fits (black) to total atomic PDFs (red) for $\text{Sm}_x\text{Bi}_{1-x}\text{FeO}_3$ ($x = 0.05, 0.1$ and $0.15, 0.2, 0.3$, and 0.4) based on structure models shown for each data set. The residual difference (blue) is shifted downward for clarity. The goodness-of-fit indicator, R_{wp} , is also shown for each data set in %. The fits are superior to those shown in Figs. S2, S3, and S4.

IV. DISCUSSION

The RMC refined large-scale atomic configurations were analyzed in terms of partial Bi-O and Bi-Fe atomic pair correlations, Fe-O-Fe bond angles, and average volume occupied by one ABO_3 formula unit, hereafter referred to as atomic volume. Results are shown in Figs. 12(a)–12(c). As can be seen in Figs. 11 and 12(a)–12(c), Bi-O pair correlations and Fe-O-Fe bond angles change considerably with Sm content reflecting the concurrent changes in the tilts of Fe– O_6 octahedra and repositioning of Bi atoms in the cavities of the perovskite lattice, leading to changes in the polarity of the crystal structure when x approaches 20% and then 40%. On the other hand, barring the overall contraction of the crystal lattice, changes in Bi-Fe pair correlations [Fig. 12(b), i.e., the mutual positioning of Bi and Fe atoms, appear less well expressed.

In particular, $\text{Sm}_x\text{Bi}_{1-x}\text{FeO}_3$ multiferroics with $x \leq 0.15$ are seen to preserve the polar structure of pure BFO in terms of an octahedral tilts pattern [see Figs. 12(c) and S6], where Bi atoms are displaced from the center of the cavities between tilted Fe– O_6 octahedra in a manner consistent with the emergence of ferroelectric order (see Fig. 11; top row). It has been shown that the spontaneous polarization, P_s , in rhombohedral BFO can be conveniently evaluated using the relationship $P_s = 258 \Delta z$ ($\mu\text{C cm}^{-2}$), where Δz is the difference between the relative displacements of Bi and Fe atoms from their positions in a hypothetical nonferroelectric BFO

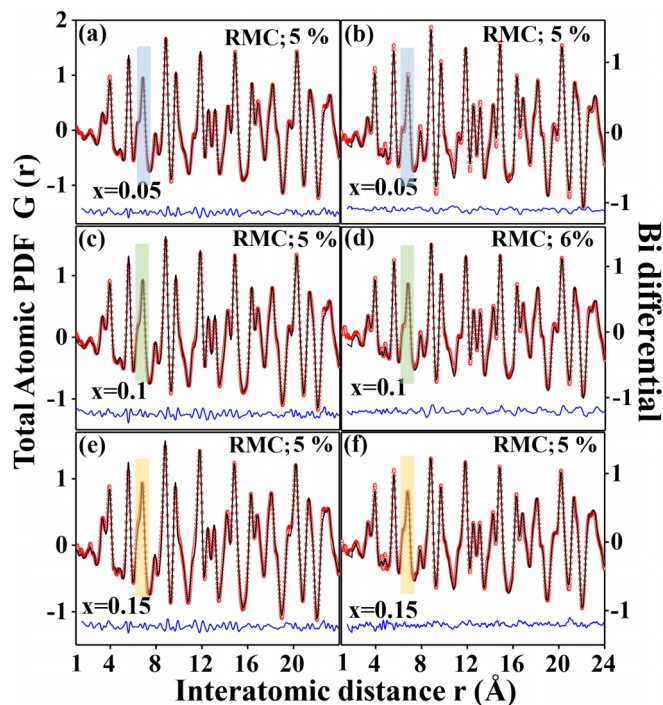


FIG. 7. RMC fits (black) to the low- r part of (a),(c),(e) total and (b),(d),(f) Bi-differential PDFs (red) for $\text{Sm}_x\text{Bi}_{1-x}\text{FeO}_3$ ($x = 0.05, 0.1$, and 0.15). The residual difference (blue) is shifted downward for clarity. The goodness-of-fit indicator R_{wp} is also shown for each data set in %. The fits are superior to those shown in Fig. 6. Colored rectangles highlight differences between respective peaks in total and Bi-differential PDFs.

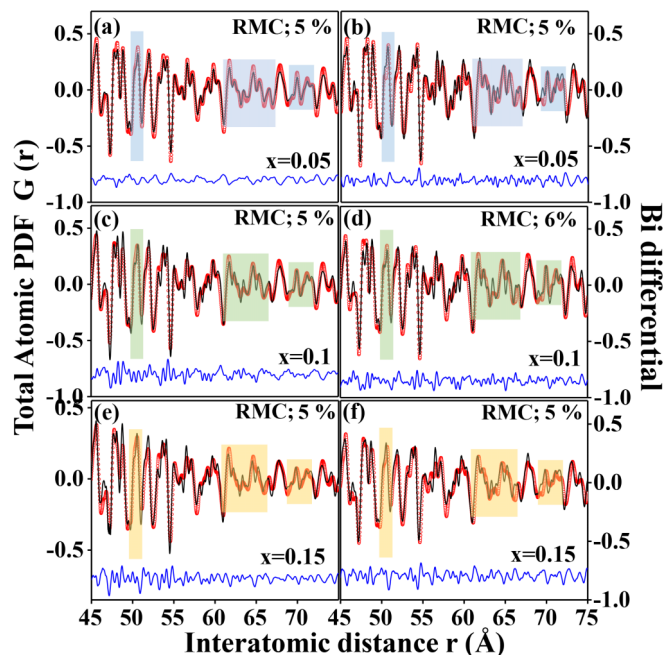


FIG. 8. RMC fits (black) to the higher- r part of (a),(c),(e) total and (b),(d),(f) Bi-differential PDFs (red) for $\text{Sm}_x\text{Bi}_{1-x}\text{FeO}_3$ ($x = 0.05, 0.1$, and 0.15). The residual difference (blue) is shifted downward for clarity. The goodness-of-fit indicator, R_{wp} , is also shown for each data set in %. Colored rectangles highlight differences between respective peaks in total and Bi-differential PDFs.

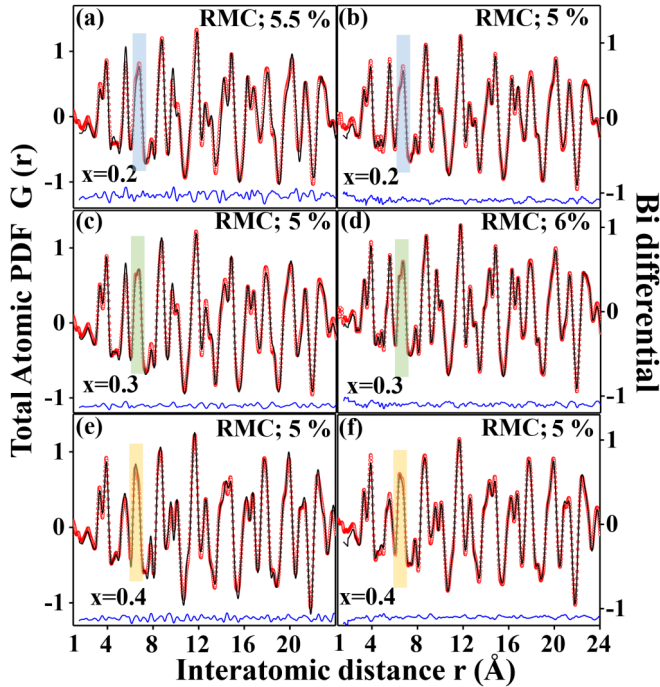


FIG. 9. RMC fits (black) to the low- r part of (a),(c),(e) total and (b),(d),(f) Bi-differential PDFs (red) for $\text{Sm}_x\text{Bi}_{1-x}\text{FeO}_3$ ($x = 0.2, 0.3,$ and 0.4). The residual difference (blue) is shifted downward for clarity. The goodness-of-fit indicator R_{wp} is also shown for each data set in %. The fits are superior to those shown in Fig. 6. Colored rectangles highlight differences between respective peaks in total and Bi-differential PDFs.

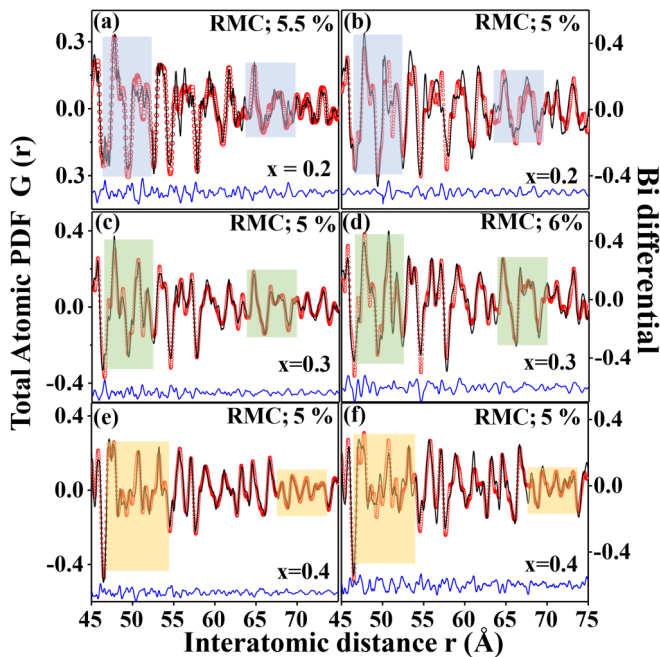


FIG. 10. RMC fits (black) to the higher- r part of (a),(c),(e) total and (b),(d),(f) Bi-differential PDFs (red) for $\text{Sm}_x\text{Bi}_{1-x}\text{FeO}_3$ ($x = 0.2, 0.3,$ and 0.4). The residual difference (blue) is shifted downward for clarity. The goodness-of-fit indicator, R_{wp} , is also shown for each data set in %. Colored rectangles highlight differences between respective peaks in total and Bi-differential PDFs.

exhibiting a centrosymmetric atomic structure. For each of the multiferroics, that difference was computed from the average positions of Bi, Fe oxygen atoms in a rhombohedral unit cell obtained by backfolding the respective RMC refined atomic configuration into the cell used to generate it initially, rendering Δz an ensemble averaged quantity. Using thus derived Δz values, we obtained an average P_s value of $98 \mu\text{C cm}^{-2}$ for pure BFO, which is in line with earlier experimental and theoretical findings [64–66]. For the Sm substituted samples we find that P_s would gradually reduce to about $71 \mu\text{C cm}^{-2}$ when x reaches 0.15, which is close to experimental results for high-quality Sm substituted BFO layers [67,68]. The results attest to the good quality of our structure study. On the other hand, the pattern of octahedral tilts [see Figs. 12(c) and S6] and Bi off-centering (see Fig. 11; bottom row) in $\text{Sm}_x\text{Bi}_{1-x}\text{FeO}_3$ ferroelectrics with $0.15 < x \leq 30$ appearing similar to those observed with other antiferroelectrics from the REFeO_3 family [29,39,58]. When the level of Sm substitution approaches $x = 0.4$, the pattern of octahedral tilts [see Figs. 12(c) and S6] and Bi off-centering (see Fig. 1; bottom row) changes further to that observed with nonpolar REFeO_3 orthoferrites, including SmFeO_3 [37,57,69]. The observation that large-scale monophasic structure models are capable of reproducing atomic pair correlations extending over more than 10 unit cells of the crystal lattice reinforces the conclusion based on crystallographic PDF analysis that $\text{Sm}_x\text{Bi}_{1-x}\text{FeO}_3$ ferroelectrics, where $0.15 < x \leq 40$, do not necessarily phase segregate, as suggested by prior Rietveld studies. The conclusion is consistent with the results of our recent study on $\text{La}_x\text{Bi}_{1-x}\text{FeO}_3$ multiferroics, which were also found to remain monophasic up to $x = 0.4$. In contrast to the case of La substituted BFO, however, $\text{Sm}_x\text{Bi}_{1-x}\text{FeO}_3$ perovskites undergo a structural transition when x approaches 0.2, where the atomic volume drops [Fig. 12(d)], the pattern of Bi displacements and octahedral tilts change [see the changes in first neighbor Bi-O distances and Fe-O-Fe bond angles in Figs. 12(a) and 12(c)], and, furthermore, the average crystal structure becomes centrosymmetric, leading to the disappearance of FE, as observed by experiment [70,71]. In the vicinity of the transition the crystal lattice is unstable, leading to a predictable increase in the electromechanical coupling and dielectric constant [37,72].

The magnetic properties of BFO follow the Goodenough-Kanamori rules [73] stating that the partially filled $3d$ orbitals of Fe atoms in perovskites would experience strong AFM exchange interactions when they form an angle of 180° . The increase in Fe-O-Fe bond angles towards 180° observed when x increases towards $x = 0.15$ [follow the arrow in Fig. 12(c)] would enhance the interactions and, hence, T_N [see Fig. 12(d)], as observed by experiment. The strengthened AFM order would weaken the spin spiral thus increasing the canted magnetic moment of Fe atoms, i.e., enhancing the weak ferromagnetism, which is consistent with the appearance of magnetic hysteresis [Fig. 1(d)] and the observed increase in the coercivity, H_c , remanent, M_r , and saturation magnetization, M_s , for $x \leq 0.15$ [Fig. 12(e)]. When x increases further, the structural distortions also increase further and $\text{Sm}_x\text{Bi}_{1-x}\text{FeO}_3$ acquires a centrosymmetric structure, i.e., becomes less anisotropic. Hence the DM interactions would vanish, leading to a destruction of the spin spiral [74], which

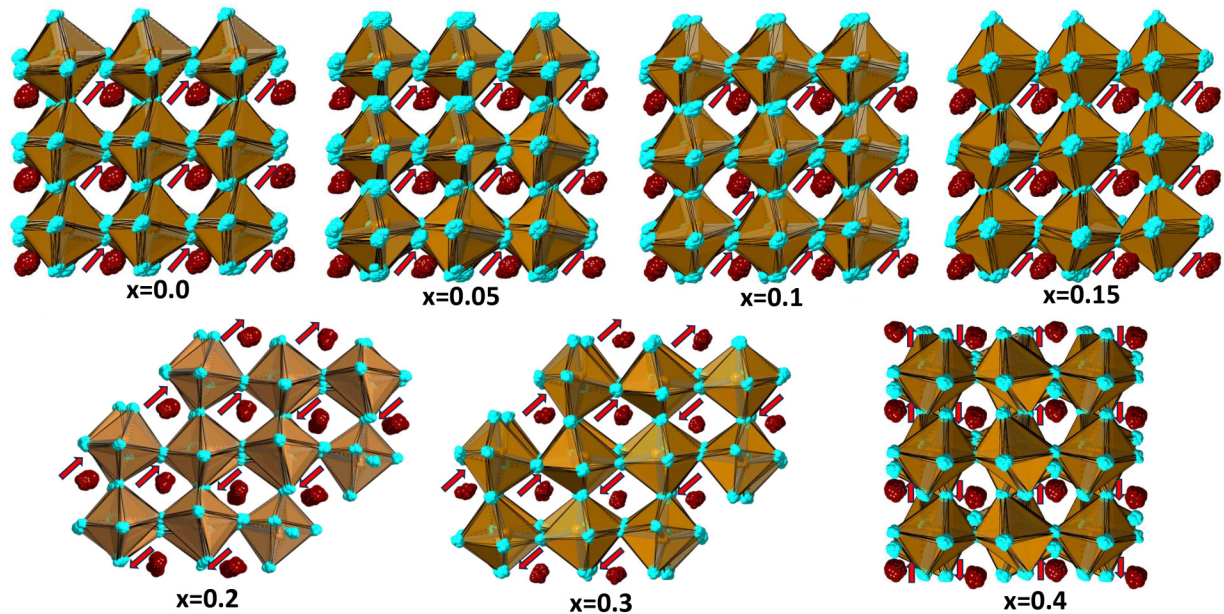


FIG. 11. Representative atomic configurations from RMC refined large-scale structure models for $\text{Sm}_x\text{Bi}_{1-x}\text{FeO}_3$ ($x = 0, 0.05, 0.1, 0.15, 0.2, 0.3,$ and 0.4) featuring a network of corner-sharing $\text{Fe}-\text{O}_6$ octahedra (brown) where Bi atoms (dark red) occupy the cavities between the octahedra. The position of each atom is an average of the positions of at least 10000 respective atoms in the RMC model. Arrows show the preferential displacement of Bi from the center of the cavities. The configurations are obtained by folding the $150 \text{ \AA} \times 150 \text{ \AA} \times 150 \text{ \AA}$ RMC models into $20 \text{ \AA} \times 20 \text{ \AA} \times 20 \text{ \AA}$ cells. Note that Sm atoms are omitted for the sake of clarity. While the atomic configurations for $x \leq 0.15$ samples are seen to exhibit one type of octahedral tilt, those for $x \geq 0.2$ samples appear to exhibit at least two distinct types of octahedral tilts.

may explain the jump in the magnetization and coercivity occurring when x approaches 0.2 [see Fig. 12(e), including the inset]. The reduced crystallographic symmetry and appearance of a broad variety of octahedral tilts, i.e., Fe-O-Fe angles (see Fig. S6), for the $x \geq 0.2$ samples may also contribute to the observed jump because it would facilitate the reorientation of Fe spins along more than one crystallographic axis when the material is subjected to an external magnetic field. Here it is to be noted that, due to thermal excitations, the end member SmFeO_3 is also known to experience a spin reorientation transition at a temperature (450 K) well below its T_N (670 K) [75]. Furthermore, it is also known that, upon heating to 1093 K, pure BFO experiences a transition from a polar $S.G.R3c$ structure to a nonpolar $S.G.Pbnm$ structure, accompanied by a 1.6% reduction in the unit cell volume [76]. Then, it appears that the structural disorder induced by the significant difference between the atomic radii of Sm and Bi atoms and that induced by thermal excitations act similarly, rendering the composition evolution of the structure and magnetic properties of Sm substituted BFO similar to the temperature evolution of the structure and magnetic properties of the end members BiFeO_3 and SmFeO_3 , respectively.

Studies have shown that most light RE substituted BFO materials exhibit a similar structural evolution with RE content, where the critical RE concentration at which the materials acquire an anti-polar structure, and thus lose FE order, appears to decrease as the RE size decreases due to the lanthanide contraction [1,20]. The observed scaling relationship between the decreasing size of RE species and stability of FE order can be conveniently expressed in terms

of decreasing $\langle r \rangle_A$ [77]. According to our results for Sm substituted BFO, the polar structure survives for $\langle r \rangle_A$ values larger than 1.356 \AA ($x \leq 0.15$ for Sm substitution), while a nonpolar structure emerges when $\langle r \rangle_A$ diminishes below 1.345 \AA ($x > 0.3$ for Sm substitution). The antipolar structure harboring AFE order appears when $\langle r \rangle_A$ is in between these values [see the color-coded phase diagram in Figs. 12(d) and 12(e)], which is in line with prior estimates [71]. The RE substitution concentration at which an antipolar structure appears may be expected to increase and decrease for RE species lighter (larger atomic size) and heavier (smaller atomic size) than Sm, respectively. For example, because $\langle r \rangle_A$ for La ($r_{\text{La}} = 1.36 \text{ \AA}$) substituted BFO would be larger than 1.356 \AA for any x , the material may be expected to never exhibit an antipolar structure, which is an experimental fact. On the other hand, for Dy ($r_{\text{Dy}} = 1.24 \text{ \AA}$) substituted BFO, the substitution window [$1.345 \text{ \AA} < \langle r \rangle_A < 1.356 \text{ \AA}$] within which the material would exhibit an antipolar structure may be expected to be between $x = 0.1$ and $x = 0.19$, which is also in line with prior estimates [78]. Data for the atomic volume can also be used to assess the structure state for BFO solid solutions when both A and B atomic species are partially substituted for others. For example, as our data for Sm substituted BFO show, an antipolar structure emerges when the atomic volume drops below 61 \AA^3 [Fig. 12(d)]. A similar critical atomic volume value for the emergence of antipolar structure has been reported for $\text{Sr}_x\text{Bi}_{1-x}(\text{Mn}_y\text{Fe}_{1-y})\text{O}_3$ [79]. The precise establishing of the concentration region for the existence of FE and AFM orders in chemically substituted BFO materials by using $\langle r \rangle_A$ and/or atomic volume as predictor

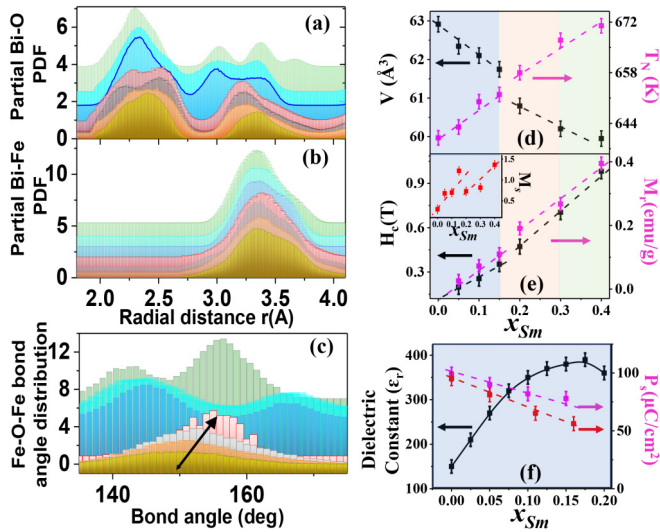


FIG. 12. (Left) Partial Bi-O (a) and Bi-Fe (b) PDFs for $\text{Sm}_x\text{Bi}_{1-x}\text{FeO}_3$ as computed from RMC refined models. Computed Fe-O-Fe bond angles are shown in (c). Data for samples with $x = 0, 0.05, 0.1, 0.15, 0.2, 0.3,$ and 0.4 are given in dark yellow, orange, gray, red, blue, cyan, and green, respectively. The arrow in (c) highlights the increase in the Fe-O-Fe bond angle, while x approaches 0.15. The presence of more than two types of Fe-O-Fe bond angles in the samples with $x \geq 0.2$, including their broad distribution, indicates the emergence of at least two distinct patterns of octahedral tilts in the antipolar and nonpolar phases of $\text{Sm}_x\text{Bi}_{1-x}\text{FeO}_3$. The latter is indeed well illustrated by the structure plots in Fig. 11. (Right) Experimental data for the atomic volume V (black symbols) and Néel temperature T_N (magenta symbols) are given in (d). Experimental data for the coercivity H_C (black symbols), remanent magnetization M_r (magenta symbols), and saturation magnetization M_s (red symbols) are given in (e). Experimental data for the dielectric constant ϵ_r (black symbols) and saturation polarization P_s (red symbols) are given in (f). Computed data for P_s (magenta symbols) are also given in (e). Light blue, red, and green rectangles highlight compositions ranging between $x = 0.0$ and $x = 0.15$, $x = 0.15$ and $x = 0.30$, and $x = 0.30$ to $x = 0.4$, where $\text{Sm}_x\text{Bi}_{1-x}\text{FeO}_3$ appears as a ferroelectric, antiferroelectric, and paraelectric, respectively.

variables may be very beneficial in the exploration of the materials for piezoelectric and high energy storage applications [37,80,81], including through machine learning techniques [82–84].

V. CONCLUSIONS

The substitution of Bi for Sm in BiFeO_3 changes the pattern of octahedral tilts and Bi displacements from polar to antipolar and then to nonpolar as the Sm to Bi ratio approaches, respectively, 0.2 and 0.4, while, likely due to cation-cation repulsion, Bi-Fe distances do not change much. The changes in the pattern of Bi displacements largely affect the polarity of the crystal lattice, i.e., spatial arrangement of electric dipoles, while that of octahedral tilts affect the magnetic order. The small changes in Bi-Fe distances may be associated with the observed weak variation of the lattice polarization with Sm content. Because of the significant lattice distortions arising from the difference in the size of substituent Sm and substituted Bi atoms, the underlying polar S.G. $R3c$, antipolar S.G. Pnm , and nonpolar S.G. $Pbnm$ structures share a common triclinic distortion, which appears to lessen phase segregation phenomena in the $0 \leq x \leq 0.4$ composition range. The results call for a reconsideration of the phase diagrams for chemically substituted perovskites in general and in particular RE-substituted BiFeO_3 , which appear to exhibit universal behavior driven by lattice distortions that can be controlled by adjusting the values for $\langle r \rangle_A$ and average atomic volume.

ACKNOWLEDGMENTS

This work was supported by the U.S. Department of Energy, Office of Science, Office of Basic Energy Sciences under Award No. DE-SC0021973 and used resources of the Advanced Photon Source at the Argonne National Laboratory provided by the DOE Office of Science under Contract No. DE-AC02-06CH11357. The help of Dr. T. Durga in preparing the samples and Dr. R. Amin in the experiments is greatly appreciated.

- [1] D. C. Arnold, Composition-driven structural phase transitions in rare-earth-doped BiFeO_3 ceramics: A review, *IEEE Trans. Ultrason., Ferroelectr. Freq. Control* **62**, 62 (2015).
- [2] M. A. Peña and J. L. Fierro, Chemical structures and performance of perovskite oxides, *Chem. Rev.* **101**, 1981 (2001).
- [3] V. A. Khomchenko, D. A. Kiselev, J. M. Vieira, L. Jian, A. L. Kholkin, A. M. L. Lopes, Y. G. Pogorelov, J. P. Araujo, and M. Maglione, Effect of diamagnetic Ca, Sr, Pb, and Ba substitution on the crystal structure and multiferroic properties of the BiFeO_3 perovskite, *J. Appl. Phys.* **103**, 024105 (2008).
- [4] H. Liu and X. Yang, A brief review on perovskite multiferroics, *Ferroelectrics* **507**, 69 (2017).
- [5] Z. Wang, Z. Shi, T. Li, Y. Chen, and W. Huang, Stability of perovskite solar cells: A prospective on the substitution of the A cation and X anion, *Angew. Chem. Int. Ed.* **56**, 1190 (2017).
- [6] B. Chen, M. Sun, R. Chen, and B. Huang, Atomic substitution effects of inorganic perovskites for optoelectronic properties modulations, *EcoMat* **4**, e12201 (2022).
- [7] A. S. Bhalla, R. Guo, and R. Roy, The perovskite structure—a review of its role in ceramic science and technology, *Mater. Res. Innov.* **4**, 3 (2000).
- [8] V. E. Zhivulin, E. A. Trofimov, S. A. Gudkova, I. Y. Pashkev, A. Y. Punda, M. Gavrilyak, M. Gavrilyak, O. V. Zaitseva, S. V. Taskaev, F. V. Podgornov, M. A. Darwish, M. A. Almessiere, Y. Slimani, A. Baykal, S. V. Trukhanov, A. V. Trukhanov, and D. A. Vinnik, Polysubstituted high-entropy $[\text{LaNd}](\text{Cr}_{0.2}\text{Mn}_{0.2}\text{Fe}_{0.2}\text{Co}_{0.2}\text{Ni}_{0.2})\text{O}_3$ perovskites: Correlation of the electrical and magnetic properties, *Nanomaterials* **11**, 1014 (2021).
- [9] J. Gunasekera, A. Dahal, Y. Chen, J. A. Rodriguez-Rivera, L. W. Harriger, S. Thomas, T. W. Heitmann, V. Dugaev, A. Ernst, and D. K. Singh, Quantum magnetic properties in perovskite with Anderson localized artificial spin-1/2, *Adv. Sci.* **5**, 1700978 (2018).
- [10] J. T. Han, Y. H. Huang, X. J. Wu, C. L. Wu, W. Wei, B. Peng, W. Huang, and J. B. Goodenough, Tunable synthesis of

- bismuth ferrites with various morphologies, *Adv. Mater.* **18**, 2145 (2006).
- [11] I. H. Lone, J. Aslam, N. R. E. Radwan, A. H. Bashal, A. F. A. Ajlouni, and A. Akhter, Multiferroic ABO₃ transition metal Oxides: A rare interaction of ferroelectricity and magnetism, *Nanoscale Res. Lett.* **14**, 1 (2019).
- [12] J. Park, S.-H. Lee, S. Lee, F. Gozzo, H. Kimura, Y. Noda, Y. J. Choi, V. Kiryukhin, S.-W. Cheong, Y. Jo, E. S. Choi, L. Balicas, G. S. Jeon, and J.-G. Park, Magnetoelectric feedback among magnetic order, polarization, and lattice in multiferroic BiFeO₃, *J. Phys. Soc. Jpn.* **80**, 114714 (2011).
- [13] M. Ramazanoglu, M. Laver, W. Ratcliff, I. I., S. M. Watson, W. C. Chen, A. Jackson, K. Kothapalli, S. Lee, S.-W. Cheong, and V. Kiryukhin, Local weak ferromagnetism in single-crystalline ferroelectric BiFeO₃, *Phys. Rev. Lett.* **107**, 207206 (2011).
- [14] A. J. Jacobson and B. E. F. Fender, A neutron diffraction study of the nuclear and magnetic structure of BiFeO₃, *J. Phys. C: Solid State Phys.* **8**, 844 (1975).
- [15] N. V. Srihari, K. B. Vinayakumar, and K. K. Nagaraja, Magnetoelectric coupling in bismuth ferrite—challenges and perspectives, *Coatings* **10**, 1221 (2020).
- [16] S. Kawachi, S. Miyahara, T. Ito, A. Miyake, N. Furukawa, J. I. Yamaura, and M. Tokunaga, Direct coupling of ferromagnetic moment and ferroelectric polarization in BiFeO₃, *Phys. Rev. B* **100**, 140412(R) (2019).
- [17] A. Agbelele, D. Sando, C. Toulouse, C. Paillard, R. D. Johnson, R. Ruffer, A. F. Popkov, C. Carretero, P. Rovillain, J.-M. Le Breton, B. Dkhil, M. Cazayous, Y. Gallais, M.-A. Measson, A. Sacuto, P. Manuel, A. K. Zvezdin, A. Barthelemy, J. Juraszek, and M. Bibes, Strain and magnetic field induced spin-structure transitions in multiferroic BiFeO₃, *Adv. Mater.* **29**, 1602327 (2017).
- [18] P. Hemme, J.-C. Philippe, A. Medeiros, A. Alekhin, S. Houver, Y. Gallais, A. Sacuto, A. Forget, D. Colson, S. Mantri, B. Xu, L. Bellaiche, and M. Cazayous, Tuning the multiferroic properties of BiFeO₃ under uniaxial strain, *Phys. Rev. Lett.* **131**, 116801 (2023).
- [19] M. D. Davydova, K. A. Zvezdin, A. A. Mukhin, and A. K. Zvezdin, Spin dynamics, antiferrodistortion and magnetoelectric interaction in multiferroics. The case of BiFeO₃, *Phys. Sci. Rev.* **5**, 20190070 (2020).
- [20] F. Mumtaz, S. Nasir, G. H. Jaffari, and S. I. Shah, Chemical pressure exerted by rare earth substitution in BiFeO₃: Effect on crystal symmetry, band structure and magnetism, *J. Alloys Compd.* **876**, 160178 (2021).
- [21] M. Połomska, B. Hilczer, I. Szafraniak-Wiza, A. Pietraszko, and B. Andrzejewski, XRD, Raman and magnetic studies of Bi_{1-x}La_xFeO₃ solid solution obtained by mechanochemical synthesis, *Phase Transit.* **90**, 24 (2017).
- [22] S. Karimi, I. M. Reaney, Y. Han, J. Pokorny, and I. Sterianou, Crystal chemistry and domain structure of rare-earth doped BiFeO₃ ceramics, *J. Mater. Sci.* **44**, 5102 (2009).
- [23] J. Wei, C. Wu, Y. Liu, Y. Guo, T. Yang, D. Wang, Z. Xu, and R. Haumont, Structural distortion, spin-phonon coupling, interband electronic transition, and enhanced magnetization in rare-earth-substituted bismuth ferrite, *Inorg. Chem.* **56**, 8964 (2017).
- [24] Y.-J. Zhang, H.-G. Zhang, J.-H. Yin, H.-W. Zhang, J.-L. Chen, W.-Q. Wang, and G.-H. Wu, Structural and magnetic properties in Bi_{1-x}R_xFeO₃ ($x = 0 - 1$, R = La, Nd, Sm, Eu and Tb) polycrystalline ceramics, *J. Magn. Magn. Mater.* **322**, 2251 (2010).
- [25] J. Dong, X. Zhang, Y. Wang, Y. Gong, P. An, H. Li, Z. Guo, X. Hao, Q. Jia, and D. Chen, Local insight into the La-induced structural phase transition in multiferroic BiFeO₃ ceramics by x-ray absorption fine structure spectroscopy, *J. Phys.: Condens. Matter* **31**, 085402 (2019).
- [26] T. Patri, A. Ghosh, M. L. V. Mahesh, P. D. Babu, S. K. Mandal, and M. N. Singh, Fortified relaxor ferroelectricity of rare earth substituted 4-layered BaBi_{3,9}RE_{0,1}Ti₄O₁₅ (RE = La, Pr, Nd, and Sm) Aurivillius compounds, *Sci. Rep.* **12**, 16508 (2022).
- [27] T. Sato, S. Takagi, S. Deledda, B. C. Hauback, and S. I. Orimo, Extending the applicability of the Goldschmidt tolerance factor to arbitrary ionic compounds, *Sci. Rep.* **6**, 23592 (2016).
- [28] Z. V. Gabbasova, M. D. Kuz'Min, A. K. Zvezdin, I. S. Dubenko, V. A. Murashov, D. N. Rakov, and I. B. Krynetsky, Bi_{1-x}R_xFeO₃ (R = rare earth): A family of novel magnetoelectrics, *Phys. Lett. A* **158**, 491 (1991).
- [29] D. A. Rusakov, A. M. Abakumov, K. Yamaura, A. A. Belik, G. V. Tendeloo, and E. T.-Muromachi, Structural evolution of the BiFeO₃-LaFeO₃ system, *Chem. Mater.* **23**, 285 (2011).
- [30] I. O. Troyanchuk, D. V. Karpinsky, M. V. Bushinsky, O. S. Mantyskaya, N. V. Tereshko, and V. N. Shut, Phase transitions, magnetic and piezoelectric properties of rare-earth-substituted BiFeO₃ ceramics, *J. Am. Ceram. Soc.* **94**, 4502 (2011).
- [31] I. O. Troyanchuk, M. V. Bushinsky, D. V. Karpinsky, O. S. Mantyskaya, V. V. Fedotova, and O. I. Prochnenko, Structural transformations and magnetic properties of Bi_{1-x}Ln_xFeO₃ (Ln = La, Nd, Eu) multiferroics, *Phys. Status Solidi B* **246**, 1901 (2009).
- [32] T. T. Carvalho, J. R. A. Fernandes, J. P. de la Cruz, J. V. Vidal, N. A. Sobolev, F. Figueiras, S. Das, V. S. Amaral, A. Almeida, J. A. Moreira, and P. B. Tavares, Room temperature structure and multiferroic properties in Bi_{0,7}La_{0,3}FeO₃ ceramics, *J. Alloys Compd.* **554**, 97 (2013).
- [33] M. M. Gomes, T. T. Carvalho, B. Manjunath, R. Vilarinho, A. S. Gibbs, K. S. Knight, J. A. Paixão, V. S. Amaral, A. Almeida, P. B. Tavares, and J. A. Moreira, Disentangling the phase sequence and correlated critical properties in Bi_{0,7}La_{0,3}FeO₃ by structural studies, *Phys. Rev. B* **104**, 174109 (2021).
- [34] V. Petkov, A. Zafar, P. Kenesei, and S. Shastri, Chemical compression and ferroic orders in La substituted BiFeO₃, *Phys. Rev. Mater.* **7**, 054404 (2023).
- [35] F. F. Orudzhev, N. M. R. Alikhanov, S. M. Ramazanov, D. S. Sobola, R. K. Murtazali, E. H. Ismailov, R. D. Gasimov, A. S. Aliev, and S. Talu, Morphotropic phase boundary enhanced photocatalysis in Sm doped BiFeO₃, *Molecules* **27**, 7029 (2022).
- [36] S. Karimi, I. M. Reaney, I. Levin, and I. Sterianou, I. Nd-doped BiFeO₃ ceramics with antipolar order, *Appl. Phys. Lett.* **94**, 112903 (2009).
- [37] X. Chen, Y. Wang, Y. Yang, G. Yuan, J. Yin, and Z. Liu, Structure, ferroelectricity and piezoelectricity evolutions of Bi_{1-x}Sm_xFeO₃ at various temperatures, *Solid State Commun.* **152**, 497 (2012).
- [38] A. Kumar and D. Varshney, Structural transition and enhanced ferromagnetic properties of La, Nd, Gd, and Dy-Doped BiFeO₃ ceramics, *J. Elect. Mater.* **44**, 4354 (2015).
- [39] Y. Horibe, M. Nomoto, T. Inoshita, K. Watanabe, S. -W. Cheong, Y. Inoue, and Y. Koyama, Quadruple superstructure

- with antiferroic ionic displacements in $\text{Bi}_{1-x}\text{Sm}_x\text{FeO}_3$, *Phys. Rev. B* **100**, 024105 (2019).
- [40] S. Saxin and C. S. Knee, Crystal structure of $\text{Bi}_{0.9}\text{Sm}_{0.1}\text{Fe}_{1-x}\text{Mn}_x\text{O}_3$ multiferroics, *Dalton Trans.* **40**, 3462 (2011).
- [41] X. X. Shi, X. Q. Liu, and X. M. Chen, Structure evolution and piezoelectric properties across the morphotropic phase boundary of Sm-substituted BiFeO_3 ceramics, *J. Appl. Phys.* **119**, 064104 (2016).
- [42] M. Nakhaei and D. S. Khoshnoud, Study on structural, magnetic and electrical properties of ReFeO_3 (Re = La, Pr, Nd, Sm & Gd) orthoferrites, *Physica B: Condens. Matter* **612**, 412899 (2021).
- [43] See Supplemental Material at <http://link.aps.org/supplemental/10.1103/PhysRevMaterials.8.124407> for DFT results and refined crystal structure data.
- [44] V. Petkov, RAD, a program for analysis of X-ray diffraction data from amorphous materials for personal computers, *Crystallography. Appl. Crystallogr.* **22**, 387 (1989).
- [45] V. Petkov and V. Buscaglia, Rhombohedral distortion and percolation phenomena in B-site substituted perovskite ferroelectrics with enhanced piezoelectric response, *Phys. Rev. Mater.* **5**, 044410 (2021).
- [46] V. Petkov, J. W. Kim, S. Shastri, S. Gupta, and S. Priya, Geometrical frustration and piezoelectric response in oxide ferroics, *Phys. Rev. Mater.* **4**, 014405 (2020).
- [47] O. Cannelli, J. Wiktor, N. Colonna, L. Leroy, M. Puppini, C. Bacellar, I. Sadykov, F. Krieg, G. Smolentsev, M. V. Kovalenko, A. Pasquarello, M. Chergui, and G. F. Mancini, Atomic-level description of thermal fluctuations in inorganic lead halide perovskites, *J. Phys. Chem. Lett.* **13**, 3382 (2022).
- [48] G. King, R. A. Ricciardo, J. R. Soliz, P. M. Woodward, and A. Llobet, Linking local structure and properties in perovskites containing equal concentrations of manganese and ruthenium, *Phys. Rev. B* **83**, 134123 (2011).
- [49] V. Petkov, T. D. Rao, A. Zafar, A. M. Abeykoon, E. Fletcher, J. Peng, Z. Q. Mao, and X. Ke, Lattice distortions and the metal-insulator transition in pure and Ti-substituted $\text{Ca}_3\text{Ru}_2\text{O}_7$, *J. Phys.: Condens. Matter* **35**, 015402 (2023).
- [50] V. Krayzman, I. Levin, J. C. Woicik, T. Proffen, T. A. Vanderah, and M. G. Tucker, A combined fit of total scattering and extended X-ray absorption fine structure data for local-structure determination in crystalline materials, *J. Appl. Crystallogr.* **42**, 867 (2009).
- [51] D. A. Keen, Perovskites take the lead in local structure analysis, *IUCrJ* **3**, 8 (2016).
- [52] B. Jones, C. Z. Suggs, E. Krivyakina, D. Phelan, V. O. Garlea, O. Chmaissem, and B. A. Frandsen, Local atomic and magnetic structure of multiferroic (Sr, Ba)(Mn, Ti) O_3 , *Phys. Rev. B* **109**, 024423 (2024).
- [53] V. Petkov, S. M. Selbach, M. A. Einarsrud, T. Grande, and S. D. Shastri, Melting of Bi sublattice in nanosized BiFeO_3 perovskite by resonant X-Ray diffraction, *Phys. Rev. Lett.* **105**, 185501 (2010).
- [54] *Novel Application of Anomalous (Resonance) X-ray Scattering for Structural Characterization of Disordered Materials*, edited by Y. Waseda (Springer, Berlin, Heidelberg, 1984).
- [55] V. Petkov and S. D. Shastri, Element-specific structure of materials with intrinsic disorder by high-energy resonant x-ray diffraction and differential atomic pair-distribution functions: A study of PtPd nanosized catalysts, *Phys. Rev. B* **81**, 165428 (2010).
- [56] V. Petkov, S. Shastri, J. W. Kim, S. Shan, J. Luo, J. Wu, and C. J. Zhong, Application of differential resonant high-energy X-ray diffraction to three-dimensional structure studies of nanosized materials: A case study of Pt-Pd nanoalloy catalysts, *Acta Crystallogr., A: Found. Adv.* **74**, 553 (2018).
- [57] S. Hu, L. Chen, Y. Wu, L. Yu, X. Zhao, S. Cao, J. Zhang, and W. Ren, Selected multiferroic perovskite oxides containing rare earth and transition metal elements, *Chin. Sci. Bull.* **59**, 5170 (2014).
- [58] I. Levin, M. G. Tucker, H. Wu, V. Provenzano, C. L. Dennis, S. Karimi, T. Comyn, T. Stevenson, R. I. Smith, and I. M. Reaney, Displacive phase transitions and magnetic structures in Nd-substituted BiFeO_3 , *Chem. Mater.* **23**, 2166 (2011).
- [59] M. Kubota, K. Oka, Y. Nakamura, H. Yabuta, K. Miura, Y. Shimakawa, and M. Azuma, Sequential phase transitions in Sm substituted BiFeO_3 , *Jpn. J. Appl. Phys.* **50**, 09NE08 (2011).
- [60] J. Rodriguez-Carvajal, FULLPROF: A program for Rietveld refinement and pattern matching analysis, in *Satellite Meeting on Powder Diffraction of the XV Congress of the IUCr, Toulouse, France* (International Union of Crystallography, Chester, UK, 1990), p. 127.
- [61] C. L. Farrow, P. Juhas, J. W. Liu, D. Bryndin, E. S. Božin, J. Bloch, Th. Proffen, and S. J. L. Billinge, PDFfit2 and PDFgui: Computer programs for studying nanostructure in crystals, *J. Phys. Condens. Matter* **19**, 335219 (2007).
- [62] V. Petkov and S. Shastri, Lattice symmetry breaking transition and critical size limit for ferroic orders in nanophase BiFeO_3 , *Phys. Rev. B* **104**, 054121 (2021).
- [63] B. Aoun, Stochastic atomic modeling and optimization with fullrnc, *J. Appl. Crystallogr.* **55**, 1664 (2022).
- [64] J. B. Neaton, C. Ederer, U. V. Waghmare, N. A. Spaldin, and K. M. Rabe, First-principles study of spontaneous polarization in multiferroic BiFeO_3 , *Phys. Rev. B* **71**, 014113 (2005).
- [65] P. Ravindran, R. Vidya, A. Kjekshus, H. Fjellvåg, and O. Eriksson, Theoretical investigation of magnetoelectric behavior in BiFeO_3 , *Phys. Rev. B* **74**, 224412 (2006).
- [66] Z. Zhong, Y. Sugiyama, and H. Ishiwara, Large remanent polarization in Sm-substituted BiFeO_3 thin film formed by chemical solution deposition, *Jpn. J. Appl. Phys.* **49**, 041502 (2010).
- [67] J. Walker, H. Simons, D. O. Alikin, A. P. Turygin, V. Y. Shur, A. L. Kholkin, H. Ursic, A. Bencan, B. Malic, V. Nagarajan, and T. Rojac, Dual strain mechanisms in a lead-free morphotropic phase boundary ferroelectric, *Sci. Rep.* **6**, 19630 (2016).
- [68] S. K. Singh, C. V. Tomy, T. Era, M. Itoh, and H. Ishiwara, Improved multiferroic properties in Sm-doped BiFeO_3 thin films deposited using chemical solution deposition method, *J. Appl. Phys.* **111**, 102801 (2012).
- [69] A. Y. Borisevich, E. A. Eliseev, A. N. Morozovska, C.-J. Cheng, J.-Y. Lin, Y. H. Chu, D. Kan, I. Takeuchi, V. Nagarajan, and S. V. Kalinin, Atomic-scale evolution of modulated phases at the ferroelectric-antiferroelectric morphotropic phase boundary controlled by flexoelectric interaction, *Nat. Commun.* **3**, 775 (2012).
- [70] N. Wang, X. Luo, L. Han, Z. Zhang, R. Zhang, H. Olin, and Y. Yang, Structure, performance, and application of BiFeO_3 nanomaterials, *Nano-micro Lett.* **12**, 1 (2020).

- [71] D. Kan, L. Pálová, V. Anbusathaiah, C. J. Cheng, S. Fujino, V. Nagarajan, K. M. Rabe, and I. Takeuchi, Universal behavior and electric-field-induced structural transition in rare-earth-substituted BiFeO₃, *Adv. Funct. Mater.* **20**, 1108 (2010).
- [72] S. Fujino, M. Murakami, V. Anbusathaiah, S. -H. Lim, V. Nagarajan, C. J. Fennie, M. Wuttig, L. Salamanca-Riba, and I. Takeuchi, Combinatorial discovery of a lead-free morphotropic phase boundary in a thin-film piezoelectric perovskite, *Appl. Phys. Lett.* **92**, 202904 (2008).
- [73] H. Weihe and H. U. Güdel, Quantitative interpretation of the Goodenough–Kanamori rules: A critical analysis, *Inorg. Chem.* **36**, 3632 (1997).
- [74] S. Pattanayak, R. N. P. Choudhary, and P. R. Das, Effect of Sm-substitution on structural, electrical and magnetic properties of BiFeO₃, *Electron. Mater. Lett.* **10**, 165 (2014).
- [75] A. A. Khan, A. Ahlawat, P. Deshmukh, R. K. Sharma, V. Srihari, R. Singh, R. Vaish, A. K. Karnal, and S. Satapathy, Effect of AFM and FM exchange interaction on magnetic anisotropy properties of single domain SmFeO₃ at nanoscale, *J. Magn. Magn. Mater.* **502**, 166505 (2020).
- [76] D. C. Arnold, K. S. Knight, F. D. Morrison, and P. Lightfoot, Ferroelectric-paraelectric transition in BiFeO₃: Crystal structure of the orthorhombic β phase, *Phys. Rev. Lett.* **102**, 027602 (2009).
- [77] Y. Yao, W. Liu, Y. Chan, C. Leung, C. Mak, and B. Ploss, Studies of rare-earth-doped BiFeO₃ ceramics, *Int. J. Appl. Ceram. Technol.* **8**, 1246 (2011).
- [78] G. Hussain, I. Ahmed, A. U. Rehman, M. U. Subhani, N. Morley, M. Akhtar, M. I. Arshad, and H. Anwar, Study of the role of dysprosium substitution in tuning structural, optical, electrical, dielectric, ferroelectric, and magnetic properties of bismuth ferrite multiferroic, *J. Alloys Compd.* **919**, 165743 (2022).
- [79] V. A. Khomchenko, M. Das, M. S. C. Henriques, and J. A. Paixão, Unusual magnetic properties of (Sr, Mn)-substituted BiFeO₃ near the polar/antipolar phase boundary, *J. Magn. Magn. Mater.* **585**, 171142 (2023).
- [80] H. Tao, J. Lv, R. Zhang, R. Xiang, and J. Wu, Lead-free rare earth-modified BiFeO₃ ceramics: Phase structure and electrical properties, *Mater. Des.* **120**, 83 (2017).
- [81] Y. Zhang, L. Bellaiche, and B. Xu, Ultrahigh energy storage density in lead-free antiferroelectric rare-earth-substituted bismuth ferrite, *Phys. Rev. Mater.* **6**, L051401 (2022).
- [82] A. Raghavan, R. Pant, I. Takeuchi, E. A. Eliseev, M. Checa, A. N. Morozovska, M. Ziatdinov, S. V. Kalinin, and Y. Liu, Evolution of ferroelectric properties in Sm_xBi_{1-x}FeO₃ via automated Piezoresponse Force Microscopy across combinatorial spread libraries, *ACS Nano* **18**, 25591 (2024).
- [83] M. Ait Tamerd, B. Abraime, A. Kadiri, A. Lahmar, M. El Marssi, M. Hamedoun, A. Benyoussef, and A. El Kenz, Prediction of magnetoelectric properties of defect BiFeO₃ thin films using Monte Carlo simulations, *J. Magn. Magn. Mater.* **539**, 168402 (2021).
- [84] D. Kan, C. J. Long, C. Steinmetz, S. E. Lofland, and I. Takeuchi, Combinatorial search of structural transitions: Systematic investigation of morphotropic phase boundaries in chemically substituted BiFeO₃, *J. Mater. Res.* **27**, 2691 (2012).